ACS APPLIED MATERIALS & INTERFACES

www.acsami.org Research Article

Surface Energy-Driven Preferential Grain Growth of Metal Halide Perovskites: Effects of Nanoimprint Lithography Beyond Direct Patterning

Jiyoung Moon, Sunah Kwon, Masoud Alahbakhshi, Yeonghun Lee, Kyeongjae Cho, Anvar Zakhidov, Moon J. Kim, and Qing Gu*

Cite This: *ACS Appl. Mater. Interfaces* 2021, 13, 5368–5378 Read Online

ACCESS | Metrics & More | Article Recommendations | Supporting Information

ABSTRACT: Hybrid organic–inorganic lead halide perovskites have attracted much attention in the field of optoelectronic devices because of their desirable properties such as high crystallinity, smooth morphology, and well-oriented grains. Recently, it was shown that thermal nanoimprint lithography (NIL) is an effective method not only to directly pattern but also to improve the morphology, crystallinity, and crystallographic orientations of annealed perovskite films. However, the underlining mechanisms behind the positive effects of NIL on perovskite material properties have not been understood. In this work, we study the kinetics of perovskite grain growth with surface energy calculations by first-principles density functional theory (DFT) and reveal that the surface energy-driven preferential grain growth during NIL, which involves multiplex processes of restricted grain growth in the surface-normal direction, abnormal grain growth, crystallographic reorientation, and grain boundary migration, is the enabler of the material quality enhancement. Moreover, we develop an optimized NIL process and prove its effectiveness by employing it in a perovskite light-emitting electrochemical cell (PeLEC) architecture, in which we observe a fourfold enhancement of maximum current efficiency and twofold enhancement of luminance compared to a PeLEC without NIL, reaching a maximum current efficiency of 0.07598 cd/A at 3.5 V and luminance of 1084 cd/m^2 at 4 V.

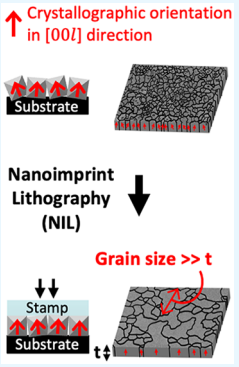

KEYWORDS: *hybrid organic–inorganic lead halide perovskites, perovskite light-emitting electrochemical cells, nanoimprint lithography, grain growth mechanism, crystallographic orientations, crystallinity, morphology, surface energy*

INTRODUCTION

Solution-processed metal halide perovskites are an emerging class of light-emitting material due to their superior optoelectronic properties, including tunable emission wavelength, large absorption coefficient, balanced ambipolar charge transport, high quantum efficiency, long carrier lifetime, and large charge carrier mobility.[1−3] In addition, they can be easily implemented in many platforms using deposition techniques such as spin coating, methylamine gas vapor annealing, and vapor-assisted/gas-assisted solution processing.[4] The above-mentioned characteristics of perovskites thus offer a cost-effective solution for device applications including lasers,[5−14] perovskite light-emitting diodes (PeLEDs),[15−17] perovskite light-emitting electrochemical cells (PeLECs),[18−20] and other optoelectronic devices.[21−38]

In lasers, for example, optical cavities that support discrete resonances are used to obtain optical modes with low lasing threshold, and these cavities are typically created by directly patterning the gain material. However, direct patterning of perovskites is known to be challenging because they degrade when exposed to polar solvents and to UV and high electron energies that are used in photo- and e-beam lithography.[39−41] As a result, optical cavities in many perovskite lasers to date are created by indirectly patterning perovskite.[6−8] This method requires the fabrication of a patterned substrate, typically by photo-/e-beam lithography, followed by spin coating of perovskites on top of the patterned substrate. In addition to poor optical mode confinement that is detrimental to high-quality laser cavities, this patterning method is relatively complicated and costly. Therefore, to create high-performance, low-cost, and highly scalable perovskite lasers and other optoelectronic devices, a strategy to directly pattern perovskites is in dire need. Several directly patterned perovskite lasers have been reported,[5,9,11,13,14] and they generally exhibit lower lasing threshold and better lasing tunability than their indirectly patterned counterparts. Patterning of perovskites has also been used to improve the performance of PeLEDs, wherein lower turn-on voltage and higher luminance were observed thanks to the increased light extraction efficiency

Received: October 1, 2020
Accepted: January 6, 2021
Published: January 21, 2021

https://dx.doi.org/10.1021/acsami.0c17655
ACS Appl. Mater. Interfaces 2021, 13, 5368–5378

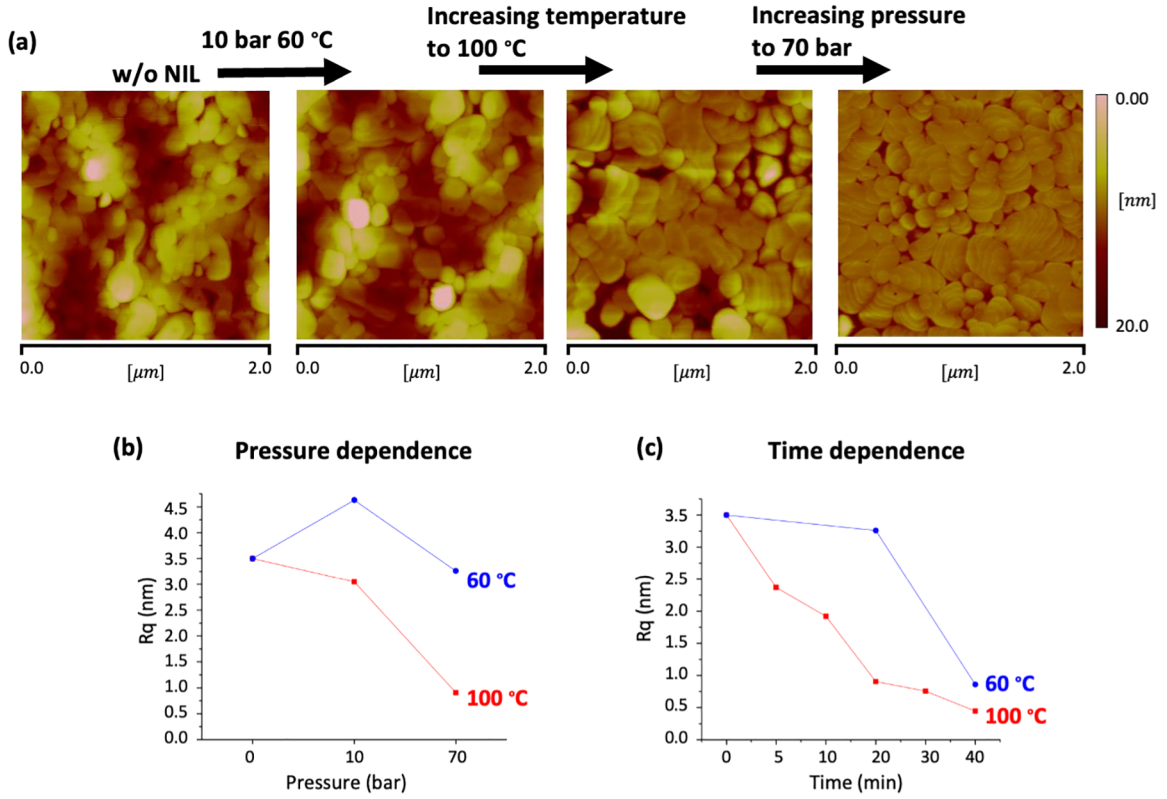

Figure 1. (a) AFM images of morphology changes in the $MAPbBr_3$ thin films due to temperature and pressure increase of NIL on the 20 nm color scale. Roughness changes of the films that are flat-imprinted at 60 °C (blue) and 100 °C (red) showing (b) pressure dependence at a constant time of 20 min and (c) time dependence at a constant pressure of 70 bar.

through patterned periodic perovskites.[17] Performance improvements have also been observed in patterned perovskite solar cells and detectors.[27,28,36] In the case of PeLECs, efficiency improvement by patterning has not been reported thus far, although similar effects to those in PeLEDs are to be expected. In fact, we find that patterning perovskites by thermal nanoimprint lithography (NIL) enhances the performance of PeLECs, as we show in a prototype PeLEC.

In terms of the direct patterning of perovskites, a number of methods have been reported. These include etching with focused-ion beam[42] or laser irradiation,[29,43] dry etching with patterned resist (etch mask),[10−12,36,37] MA gas-assisted soft-NIL,[17] and solvent-assisted soft-NIL[28,35,44] or hard-NIL.[5,9,13,27,45] Typically, soft-NIL is performed on unannealed films with a soft polymer stamp (e.g., Polydimethylsiloxane (PDMS)), while hard-NIL is performed on annealed films with a hard stamp (e.g., Si). When applied on annealed perovskite thin films, hard-NIL was reported to improve crystallographic orientation, crystallinity, and morphology and to increase grain size of perovskite, in addition to enabling the formation of fine features directly on the perovskite.[5,9,13,14,45−47]

NIL was first introduced by Chou et al. in 1995 as a cost-effective patterning alternative to e-beam/photolithography of thermoplastic polymer spin coated on a substrate.[48] Typically, NIL is performed at a temperature above the glass transition point of the particular polymer under elevated pressure while the polymer is in contact with a stamp (most often a Si or SiO_2 stamp in the hard-NIL configuration). After cooling the NIL system and demolding the stamp from the polymer, a negative replica of the stamp is formed. Because NIL is performed on the sacrificial polymer (etch mask) rather than on the material to be patterned by subsequent etching, the property changes of the polymer during NIL is not of interest and therefore often ignored. Instead, the volume exchange of the polymer in relation to the stamp dimension is usually studied to ensure repeatable NIL processes because every polymer has its unique glass transition temperature and temperature-dependent viscoelasticity. In contrast to polymers, perovskites do not have glass transition temperature. They have high melting temperatures exceeding 300 °C and typically decompose before melting[49] or in conjunction with melting.[50] Perovskites also chemically react with moisture and O_2 in the environment. Consequently, NIL of perovskites is much more challenging. Nonetheless, NIL of perovskites has been demonstrated, and improvements in crystallographic orientation, crystallinity, and morphology during NIL were shown.[5,9,13,14,45−47] To unravel the underlining mechanisms behind the enhancement of polycrystalline perovskite thin film qualities through NIL and, furthermore, to optimize NIL conditions for perovskites, the kinetics of perovskite grain growth during NIL needs to be understood. Grain growth has been studied in metals, ceramics, and semiconductors, and the mechanism can be applied to other materials that have grains. Although perovskite grain growth has been studied,[24,30−34] the studies thus far all focus on effects of composition and deposition methods.

In this work, we investigate grain growth in post-deposition perovskite thin films for the first time. Specifically, we describe the effects of NIL on the preferential grain growth of annealed methylammonium lead bromide ($MAPbBr_3$) films using classical grain growth mechanisms with surface energy calculations by first-principles density functional theory (DFT) and systematically investigate how different NIL

https://dx.doi.org/10.1021/acsami.0c17655
ACS Appl. Mater. Interfaces 2021, 13, 5368−5378

parameters influence the morphology, crystallinity, and crystallographic orientations of $MAPbBr_3$. Morphology including grain size, roughness, and the number of defects (e.g., pinholes) are examined by scanning electron microscopy (SEM), atomic force microscopy (AFM), and atomic-resolution scanning transmission electron microscopy (STEM). Crystallinity and crystallographic orientations are analyzed by the omega rocking curve, out-of-plane, in-plane, and pole figure X-ray diffraction (XRD) studies. Surface energy in different crystallographic orientations is studied by first-principles DFT calculations. Lastly, we apply NIL to a prototype PeLEC and observe a fourfold enhancement of maximum current efficiency and twofold enhancement of luminance as a result of the preferential grain growth during NIL.

RESULTS AND DISCUSSION

In this work, we choose spin-coated $MAPbBr_3$ films on Si substrates that have been annealed at 70 °C for 5 min(i.e., pre-crystallized films). To study the effect of NIL temperature, time, and pressure on perovskite properties, we use an unstructured Si stamp (i.e., flat-NIL). See the details of film preparation and different NIL processes in the Methods.

Restricted Grain Growth in the Surface-Normal Direction. Figure 1 summarizes the temperature and pressure effects on the densification and surface flattening from NIL (schematically shown in Figure S1b). As shown by the AFM images in Figure 1a, we find 60 °C NIL at 10 bar for 20 min to be ineffective since this process results in a rougher surface (Rq = 4.63 nm) than the control sample (a film without NIL, with Rq = 3.5 nm). As temperature is increased from 60 to 100 °C at a relatively low pressure of 10 bar, plateau-like grains are observed. We attribute this morphology improvement to the molding of perovskite grains by NIL at the elevated 100 °C, despite the low pressure. Upon increasing pressure to 70 bar at 100 °C in the surface-normal direction—a condition that amplifies the restricted grain growth—more plateau-like grains, densification of thin films, and smoother surfaces are observed. The restricted grain growth in the surface-normal direction densifies the surface, while that in the surface-parallel direction enlarges grains and reduces the amount of grain boundaries. If the 60 °C process is performed for a longer time (40 min) or at a higher pressure (70 bar), as shown in Figure S2a, similar effects as those at 70 bar and 100 °C, namely, plateau-like grains, densification of thin films, and a smoother surface can be seen, although it is not as effective as 100 °C. This implies that at 60 °C, $MAPbBr_3$ is not soft enough to benefit from the flattening effect by NIL under the low pressure of 10 bar and the relatively short time of 20 min. Further discussion of morphology change as a function of temperature, pressure, and time can be found in the Supporting Information Part A.

Figure 1b,c depicts the dependence of film roughness on pressure and time, respectively. AFM images as a function of pressure and time at a constant temperature of 60 or 100 °C can be found in Figure S2. We compare these results to a film without NIL, which is presented as 0 bar in Figure 1b and 0 min in Figure 1c. As discussed earlier, both 60 and 100 °C processes produce the smoothest surface at the highest pressure of 70 bar. Under these conditions, a smoother surface (i.e., smaller Rq) is observed with increasing time. We note that NIL for 20 min is most effective with 74.1% roughness reduction. By doubling the time to 40 min, only an additional 13.1% roughness reduction is observed at the expense of worsened crystallographic orientation (discussed in the "Crystallographic Reorientation and Crystallization").

Abnormal Grain Growth. Solution-processed perovskite thin films typically have a polycrystalline structure that consists of single crystals (termed as grains in polycrystals) surrounded by interfaces (termed as grain boundaries). Grain boundaries have higher energies than neighboring grains, which makes the system thermodynamically unstable. Therefore, grain boundaries become a driving force for enlarging the grain size in an attempt to reduce the total grain boundary area and thus energy. As grains grow, grain size increases by temperature-dependent grain boundary diffusion while maintaining a uniform size distribution—a phenomenon called as normal grain growth. However, if a subset of grains grows at a faster rate than neighboring grains, different (i.e., bimodally distributed) grain sizes result—a phenomenon called as abnormal grain growth or discontinuous grain growth. Abnormal grain growth has been observed in perovskite polycrystalline thin films[51,52] but is more prominent during NIL. Figure 2a depicts the concept of such abnormal grain growth mechanism during NIL. Figure 2b shows SEM images of the $MAPbBr_3$ thin film before undergoing NIL, in which we observe fiber-like microstructures where the grain size in the surface-normal direction (d_n) is similar to the thin-film

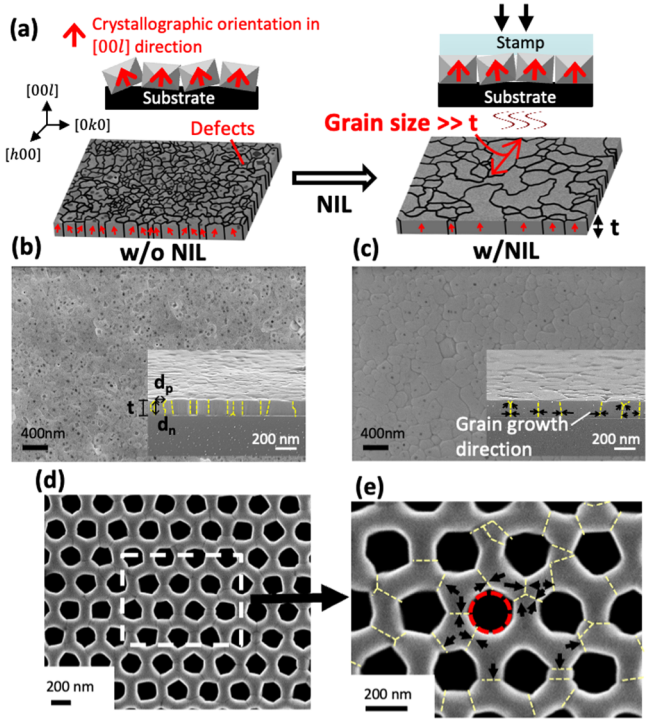

Figure 2. (a) Grain growth mechanism during NIL, illustrated by schematics of crystallographic reorientation (top) and abnormal grain growth (bottom) with grain size larger than thickness of the film (t). SEM images of $MAPbBr_3$ thin films (b) without and (c) with NIL (inset: cross-section SEM). d_p = grain size in the surface-parallel direction, d_n = grain size in the surface-normal direction, and t = thickness of the film. (d) SEM image of a patterned $MAPbBr_3$ thin film by NIL with a 2D nanopillar stamp. (e) Zoom-in image showing the effect of grain boundaries during NIL, which hinder a perfect negative replica of the pillar stamp. Yellow dotted lines are overlaid over grain boundaries to provide visual aid. Black arrows next to grain boundaries indicate the grain growth direction during NIL. The red dotted circle marks the dimension of the stamp.

https://dx.doi.org/10.1021/acsami.0c17655
ACS Appl. Mater. Interfaces 2021, 13, 5368−5378

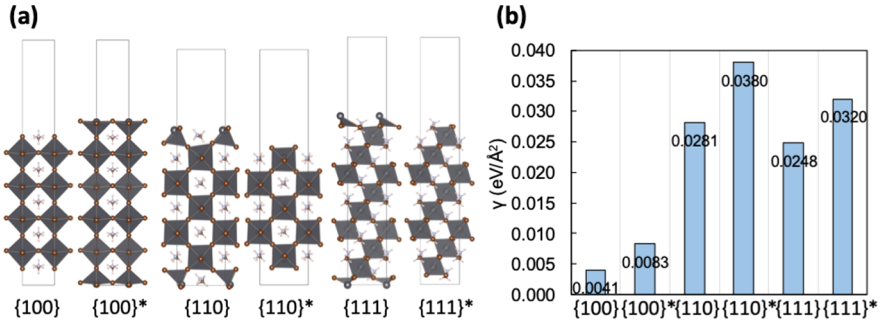

Figure 3. First-principles DFT calculation of surface energies of different crystallographic orientations and surface cleavages. (a) Slab geometries modeled for the surface energy calculation. The asterisk is an index for a surface configuration with a higher energy than the other. (b) Calculated surface energies under the Br-poor and Pb-rich conditions.

thickness ($t \cong 190$ nm). The films with fiber-like microstructures (i.e., $d_n \cong t$) experience slowing down of the grain growth rate due to the lack of grain boundaries in the surface-normal direction. During NIL, in addition to the growth restraint due to the fiber-like microstructures from the initial film, the applied surface-normal pressure further restrains grain growth in the surface-normal direction, while that in the surface-parallel direction is promoted. We find enlarged grains with bimodal distribution (Figure S11), non-equiaxed grain shapes (i.e., the length of a grain in one direction is much longer than that in the other direction), shrinkage of pore size, and reduction in the number of pores between and within grains (see the SEM image in Figure 2b,c and atomic-resolution STEM image in Figure S10), all through grain boundary migration during NIL. It can therefore be concluded that perovskites under NIL experience abnormal grain growth with bimodal grain size distribution, during which the growth rate becomes temporarily time-dependent and strongly crystallographic orientation-dependent.

As many perovskite optoelectronic devices require patterned perovskites, we also study the grain boundary migration beyond the flattening effect by NIL. Figure 2d shows the SEM image of a patterned $MAPbBr_3$ thin film with a 2D nanopillar stamp (with dimensions of 600 nm period, 165 nm diameter, and 150 nm height), and Figure 2e illustrates how grain boundaries migrate during patterning by NIL. Patterning by NIL should ideally produce a negative replica of the stamp, namely, circles with round edges as marked by the red dotted circle. Instead, hexagonal-shaped holes form, suggesting that grain boundaries are the limiting factor that hinders the perfect negative replica of the stamp. Note that even with the same stamp and NIL procedure, different perovskite compositions show varying patterning results, reinforcing the need to understand the fundamental cause of material changes under different NIL conditions.

During abnormal grain growth, grains orient to have the lowest surface energy dominate the growth.[51,52] To evaluate the lowest surface energies of grains with different crystallographic orientations, we determine the chemical potentials and perform first-principles DFT calculations. Given the measured Br/Pb atomic percentage ratio of 2.47−2.6:1 [see Figure S13 for experimental details on transmission electron microscopy−energy dispersive X-ray spectroscopy (TEM−EDX) and Figure S14 for X-ray photoelectron spectroscopy (XPS) analysis of the $MAPbBr_3$ thin film], which deviates from the stoichiometric ratio of 3:1 (Br/Pb), Br-poor and Pb-rich conditions are specified in the calculation (see the Methods for calculation details). For the {100}, {110}, and {111} family of planes, the surfaces are cleaved in two different ways, as shown in Figure 3a,b shows the calculated surface energies of these orientations. Because the lowest surface energy is found to be the {100} family of planes, grains with (001) orientations are energetically favorable in growth. These calculation results match the experimental data well. Experimentally, (001) texture is further developed after NIL, which means that grains with less deviation from the average orientation of (001) planes in the surface-normal direction grow faster.

The pressure dependence study by NIL shows that the applied surface-normal pressure aids the abnormal grain growth, which then leads to the development of (001) texture through the synergetic processes of crystallographic reorientation to the [001] direction and grain boundary migration, observed by morphology and orientation analysis through multiplex XRD techniques and SEM/AFM/STEM. Because of the random crystallographic orientations of grains in the surface-parallel direction, the direction of grain boundary migration and crystallographic reorientation varies from one grain to another, thus affecting the grain growth rate of individual grains. In turn, the grain growth rate becomes probabilistic rather than deterministic during the abnormal grain growth amplified by NIL. When the grain sizes of the fiber-like microstructures (i.e., $d_p < d_n \cong t$) in the surface-parallel direction (d_p) increase and become similar to those in the surface-normal direction (d_n), columnar structures are formed (i.e., $d_p \cong d_n \cong t$) and the grain growth is strongly dependent on the surface energies of grains (i.e., abnormal grain growth). Under this circumstance, grains orient themselves, such that those with low surface energies dominate the growth. As a result, a subset of grains ends up having much larger sizes than their neighboring grains (i.e., grain size $\gg t$ for a subset of grains, as schematically shown in Figure 2a). Due to the fluctuation in relative grain size and the development of columnar structures (i.e., $d_p \cong d_n \cong t$) that lead to surface energy-driven abnormal grain growth, we find that grain sizes do not noticeably increase as NIL time increases. This is consistent with the classical grain growth mechanism, in which the driving force for grain growth reduces as the grain size in the surface-parallel direction (d_p) becomes greater than that in the surface-normal direction (d_n), which is a result of the abnormal grain growth process. We also observe the grain growth to be dependent on the NIL temperature: the abnormal growth rate is higher at 120 °C than at 60 or 100 °C. At 120 °C, the difference between the largest and smallest grain sizes is largest and the fluctuation in relative grain size is

https://dx.doi.org/10.1021/acsami.0c17655
ACS Appl. Mater. Interfaces 2021, 13, 5368−5378

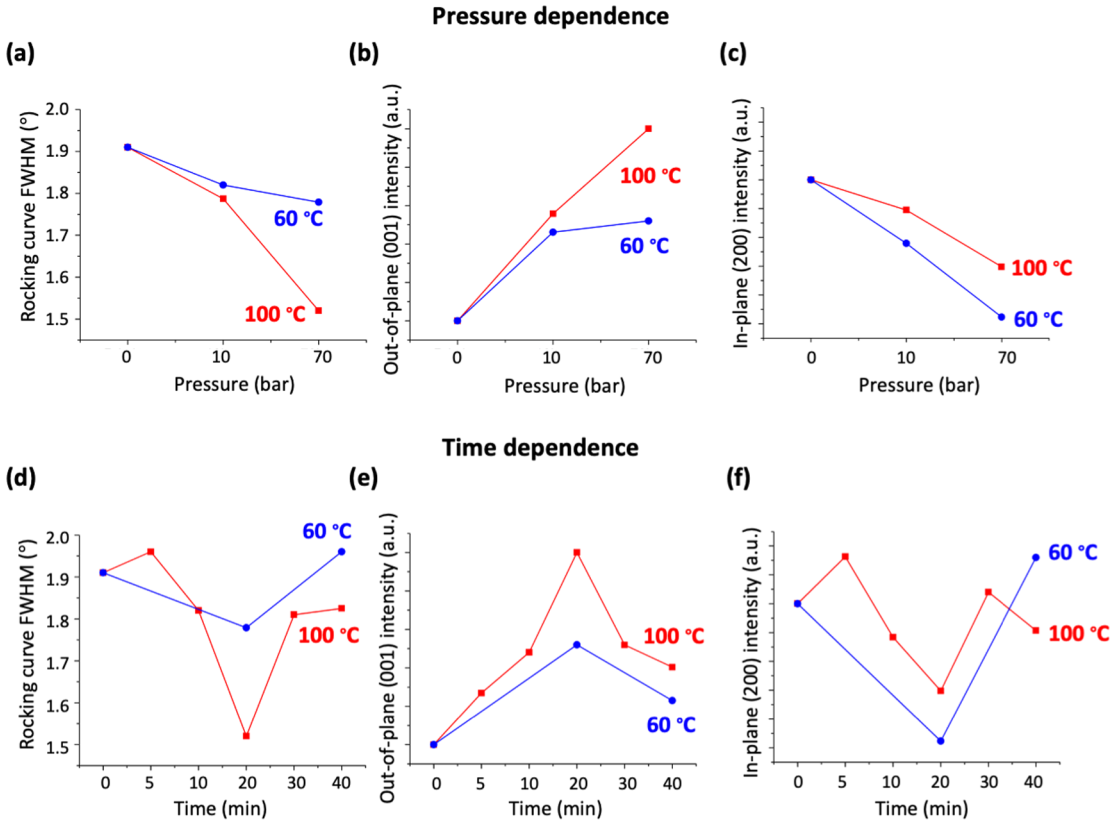

Figure 4. Pressure dependence at constant time (a–c) and time dependence at constant pressure (d–f) at 60 and 100 °C NIL; (a,d) (001) plane rocking curve FWHM, (b,e) out-of-plane (001) intensity, and (c,f) in-plane (200) intensity.

most severe (e.g., the largest grain size is tens of micrometers and smallest grain size is a few hundred nanometers, as shown in Figure S4), which is a consequence of the larger grain boundary mobilities at higher temperatures.[51] Although the grain growth rate is higher at 120 °C than at 60 and 100 °C, we find that the same pressure and time at 120 °C yield unreproducible morphology (e.g., grain size) and large fluctuation in relative grain sizes with different NIL time periods (e.g., 5 min produces larger grain size than 10 min but smaller grain size than 20 min), possibly due to the excessive abnormal grain growth phenomenon under these conditions. Further discussion can be found in the Supporting Information Part B.

Crystallographic Reorientation and Crystallization. Because XRD counts depend on the number of planes that comprise the periodic array of atoms, a higher XRD peak intensity implies two possibilities, namely, more preferred crystallographic orientation or enhanced crystallization. As shown in Figure S10, out-of-plane measurements show that compared to without NIL, higher XRD peak intensities from the {100} family of planes are seen after NIL, indicating either enhanced preferred orientation or crystallization or both.

To study the effect of NIL on the preferred crystallographic orientation alone, we also perform rocking curve XRD measurements that quantify the degree of deviation from their average orientation. This is accomplished by scanning a range of omega angles with a fixed two-theta angle that corresponds to the diffraction plane of interest. Because out-of-plane and in-plane measurements with the same scan range (2θ = 5–60°) show uniaxial texture of $MAPbBr_3$ films consisting of the {100} family of planes in the surface-normal direction while having random orientations in the surface-parallel direction (see out-of-plane and in-plane XRD measurements in Figure S8), we measure the degree of (001) texture in all $MAPbBr_3$ thin films. Note that an out-of-plane pre-measurement is required before omega rocking curve measurements in order to find the precise 2θ angle at which (001) planes of $MAPbBr_3$ films diffract since interplanar spacings of each film may not be the same. Figure 4 summarizes the omega rocking curve, out-of-plane, and in-plane XRD studies on preferred crystallographic orientation and crystallinity, under 60 and 100 °C NIL conditions. To study the pressure dependence, the processing time is first fixed at 20 min. Omega rocking curve results in Figure 4a show that more (001) textured grains form as pressure increases, as the full-width half maximum (FWHM (deg)) decreases from 1.91 to 1.779° (at 60 °C) and to 1.52° (at 100 °C). Out-of-plane measurements show increasing (001) peak intensity with increasing pressure (Figure 4b), in which the 100 °C conditions have a more rapid increase in (001) peak intensity than 60 °C. In the in-plane XRD measurements, we observe a decreasing intensity of the (200) peak with increasing pressure (Figure 4c), in which the 60 °C conditions show a more rapid decrease in peak intensity than 100 °C. The abovementioned results suggest that the 100 °C conditions with increasing pressure enhance crystallization in both surface-normal and surface-parallel directions, with more crystallographic reorientation in the surface-normal direction in comparison with the 60 °C conditions.

Next, we examine the time dependence of 60 and 100 °C processing conditions at a fixed pressure of 70 bar. For both temperatures, as the processing time increases from 20 to 40 min, we observe a wider rocking curve FWHM (Figure 4d),

https://dx.doi.org/10.1021/acsami.0c17655
ACS Appl. Mater. Interfaces 2021, 13, 5368–5378

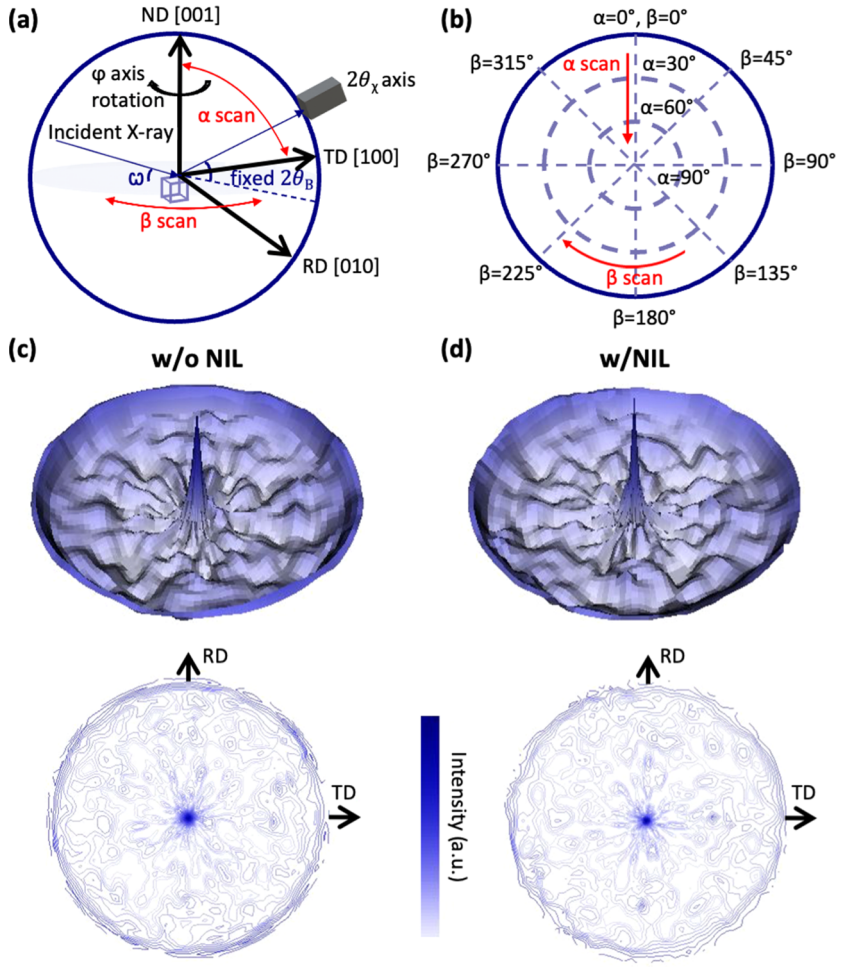

Figure 5. (a) Schematic of pole figure measurement. (b) Stereographic projection. Pole figure measurements on films (c) without and (d) with NIL.

lower (001) peak intensity (Figure 4e), and higher (200) peak intensity (Figure 4f). The 60 °C conditions show even wider rocking curve FWHM, lower (001) peak intensity, and higher (200) peak intensity compared to 100 °C. In terms of enhancement of the crystallinity and uniaxial texture in the surface-normal direction, the results indicate that 100 °C is more optimal than 60 °C and 20 min is more optimal than 40 min. Therefore, at the more optimal 100 °C, we further examine the effect of time. The FWHM increases from 1.91 to 1.96° with 5 min NIL, while both (001) and (200) peak intensities increase. This shows that compared to the film without NIL (represented as 0 min), the grains become less oriented in the surface-normal direction, while crystallinity improves. As the time increases to 10 min, FWHM decreases to 1.82°, (001) peak intensity increases, and (200) intensity decreases. At 20 min, FWHM further decreases to reach the minimum value of 1.52°, (001) peak intensity reaches the maximum value, and (200) intensity reaches the minimum value, suggesting 20 min to be the critical time to obtain well-oriented grains with crystallinity enhancement. After passing the critical time (20 min), FWHM increases again and (001) peak intensity decreases, while (200) peak fluctuates (higher at 30 min and lower at 40 min). Such fluctuation as a function of time implies that grains reorient themselves during the abnormal grain growth. We explain this phenomenon by considering $MAPbBr_3$ to be composed of "A" and "B" grains, in which an "A" grain resides in a matrix of "B" grains. The "A" grain orientation [less deviation from the average orientation of the (001) plane] has the lower surface energy and thus grows at a faster rate, whereas the matrix of "B" grain orientation [more deviation from the average orientation of the (001) plane] has the higher surface energy and grows at a slower rate. As a result, the "A" grain with a faster growth rate grows by consuming atoms in the neighboring "B" grains. To further reduce the surface and interface (e.g., grain boundary) energy in the system, over time, crystallographic reorientation can occur during the growth, which results in the development of restricted crystallographic orientations.[53] The {100} family of planes has the lowest surface energy according to the first-principles DFT calculations, which means that grains with the (00*l*) orientation (in the surface-normal direction) or (*h*00) orientation (in the surface-parallel direction) have the lowest surface energy. The active crystallographic reorientation is observed by both out-of-plane and in-plane XRD, showing fluctuation of (001) and (200) peak intensities in the time-dependent study at constant temperature (Figure 4d–f).

While the time-dependent study reveals 20 min to be the critical time for developing highly oriented grains in the surface-normal direction, we conducted pole figure XRD measurements to further understand the development of uniaxial texture (before and after 20 min NIL) in the three-dimensional space. The pole figure measurement, schemati-

https://dx.doi.org/10.1021/acsami.0c17655
ACS Appl. Mater. Interfaces 2021, 13, 5368–5378

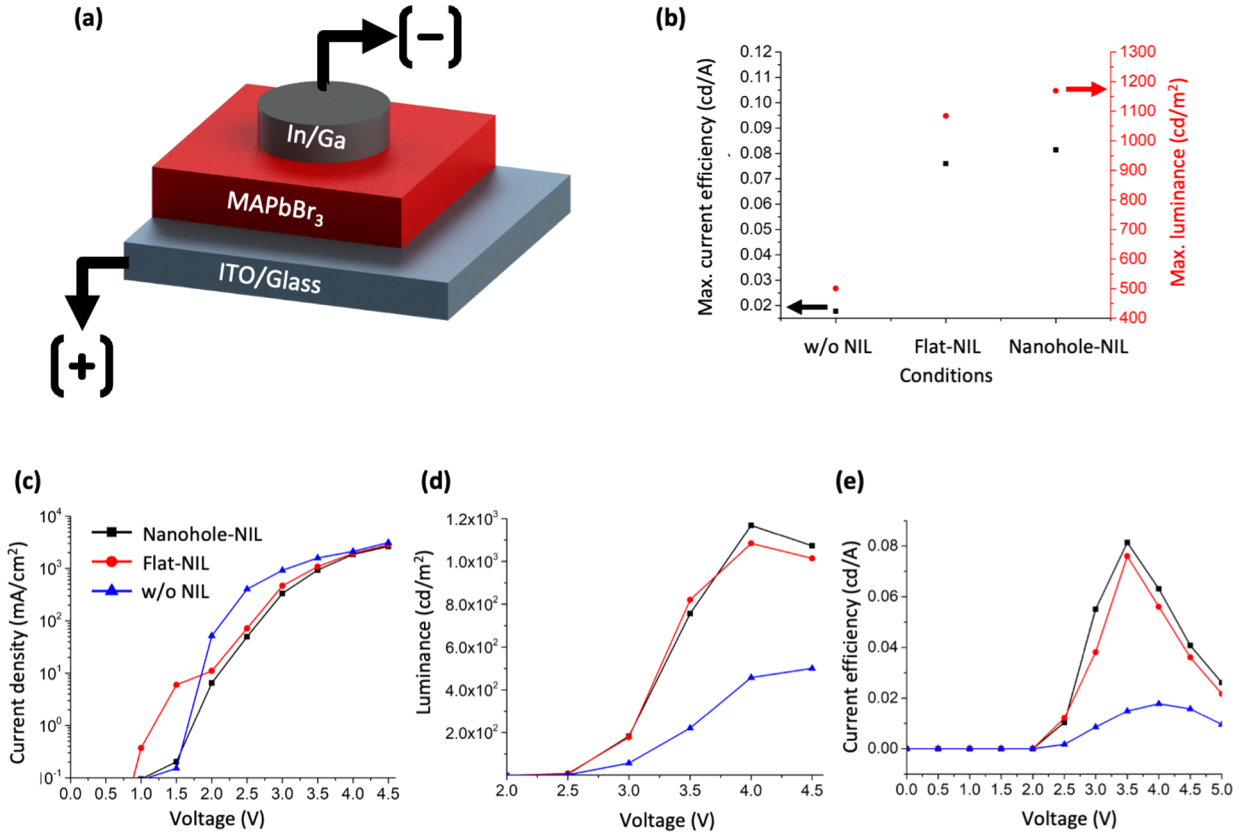

Figure 6. (a) Schematic of the $MAPbBr_3$ LEC structure. (b) Max. current efficiency and luminance of three different conditions in the $MAPbBr_3$ film. (c) Current density−voltage (J−V), (d) luminance−voltage (L−V), and (e) current efficiency−voltage characteristics without NIL (blue line), with flat-NIL PeLEC (red line), and with nanohole-NIL PeLEC (black line).

cally shown in Figure 5a, is an effective investigative XRD technique for studying the distribution of crystallographic orientations.[54] Diffracted X-rays are collected at a fixed 2θ angle—that corresponds to a certain diffraction plane—while varying the β angle (0−360°) at different α angles. The results are then plotted on stereographic projection (Figure 5b). We employ the in-plane measurement method, which does not tilt the sample to change the α angle but instead tilts the $2\theta\chi$ axis.[55] The pole figures of the (002) plane in both with and without NIL films are obtained by collecting the XRD intensity with a fixed 2θ of 30.13°. The resulting stereographic projections are shown in Figure 5c,d in 3D (top) and 2D (bottom). The pole figure would exhibit no apparent feature for polycrystalline films with randomly oriented grains but would exhibit only dots or a mixture of dot(s) and ring(s) for highly textured films. Both with and without NIL conditions yield a single dot at α = 90° with a continuous ring at α = 0°, suggesting uniaxial texture in the surface-normal direction. There are also distinct differences. The dot from the NIL film is smaller in size and higher in intensity, corresponding to a higher degree of crystallographic orientation and crystallinity in the surface-normal direction. On the other hand, weaker ring intensity is observed in the NIL film, indicating that the crystallographic orientation varies more in the surface-parallel direction.

PeLEC Performance Enhancement. To evaluate the effect of preferential grain growth on device performance, we study the PeLEC due to its simple architecture. Different from PeLEDs, PeLECs do not have electron and hole transport layers, and the motion of ions in perovskites determines the current efficiency and brightness. Therefore, this simple architecture provides a good platform to study how the electrical and optical properties of PeLECs are affected by NIL. As shown in Figure 6a, the PeLEC consists of perovskites as an ionic emitting layer, a top InGa cathode, and a bottom indium tin oxide (ITO) anode.[18,20] Under bias, ions in perovskites drift to the electrodes and create p−i−n junctions at the interfaces. The accumulation of ions at the interfaces creates electric double layers (EDLs) at both sides of the perovskite layer, reducing the potential barriers at the interfaces and, in turn, assisting the injections of carriers. It is known that characteristics of ion motion are strongly dependent on the crystallinity and grain size of perovskite films.[18] With improved crystallinity and larger grain size, more ions can travel to the electrodes with reduced loss and increased mobility, thus creating more balanced EDLs. The balanced carriers from the EDLs can soar up the luminance and current efficiency of PeLECs.

In this study, two PeLECs with the optimal NIL conditions, namely, 100 °C, 70 bar, and 20 min(see further discussion about the effectiveness of 100 °C, 70 bar, and 20 min NIL in the Supporting Information Part D), are fabricated using a flat stamp and a 2D nanopillar stamp, and their performance is compared with that of a control PeLEC that did not go through NIL. Figure 6b shows the maximum luminance and current efficiency under the three different conditions. Due to the enhanced radiative recombination rate through material quality improvements during NIL, the flat-NIL PeLEC shows fourfold enhancement of maximum current efficiency and twofold enhancement of luminance compared to the PeLEC

https://dx.doi.org/10.1021/acsami.0c17655
ACS Appl. Mater. Interfaces 2021, 13, 5368−5378

without NIL, reaching a maximum current efficiency of 0.07598 cd/A at 3.5 V and luminance of 1084 cd/m^2 at 4 V. With the 2D nanopillar stamp, thanks to the increased light scattering from patterned $MAPbBr_3$, the maximum current efficiency and luminance of nanohole-NIL PeLEC are further enhanced to 0.0813 cd/A at 3.5 V and 1169 cd/m^2 at 4 V, respectively. Note that we used the commercially available 2D nanopillar stamp in the nanohole-NIL PeLEC fabrication, and we expect even larger enhancement of efficiency and luminance with customized stamps whose dimensions are tailored for $MAPbBr_3$ resonance. The current density, luminance, and current efficiency as a function of voltage are shown in Figure 6c–e. The current density is lower (Figure 6c) and luminance is higher (Figure 6d) after 2.5 V (with turn-on voltage between 2.0 and 2.5 V), which results in higher current efficiency shown in Figure 6e. Although MA halide perovskites are not optimal for electrically driven operations due to inherent instability from the organic component methylammonium, our result clearly proves the effectiveness of NIL in improving perovskite quality and in direct patterning of perovskite and, ultimately, device performance.

CONCLUSIONS

We demonstrate that NIL amplifies surface energy-driven preferential grain growth in $MAPbBr_3$ thin films, which involves multiplex processes of restricted grain growth in the surface-normal direction, abnormal grain growth, crystallographic reorientation, and grain boundary migration. This is distinctively different from the grain growth during spin coating of the films. By studying the NIL processing temperature, pressure, and time effect on perovskite qualities including surface morphology, texture, and crystallinity, we provide benchmarks on how to optimize the NIL process with in-depth understanding of grain growth during NIL. We find that NIL induces further (001) texture development in $MAPbBr_3$ thin films, consistent with the first-principles DFT calculation results. Applying the optimized NIL process to a prototype PeLEC, we show that the PeLEC performance is improved. Furthermore, the ability to shape, smooth, and increase texture and crystallinity of perovskites demonstrates that NIL is a promising fabrication method for many perovskite optoelectronic devices, including light sources, photodetectors, and solar cells.

METHODS

Sample Preparations. $MAPbBr_3$ one molarity (1 M) solution is first prepared by dissolving 1:1 molar ratio of MABr (GreatCell solar):$PbBr_2$ (Alfa Aesar) in a 7:3 volume ratio of γ-butyrolactone (GBL) (from Sigma Aldrich): dimethyl sulfoxide (DMSO) (from Sigma Aldrich) solvent mixture at room temperature for 48 h, and filtering of the solution is performed with a 0.45 μm PTFE syringe filter. $MAPbBr_3$ thin films with a thickness of 190 nm are prepared on an immaculate substrate (e.g., Si or ITO/glass) using an anti-solvent assisted spin-coating method (step 1: 1000 revolutions per minute (rpm) for 15 s, step 2: 5000 rpm for 30 s, and dropping of 300 μL of anhydrous toluene at 15 s into step 2). All the films are annealed at 70 °C for 5 min prior to NIL. The $MAPbBr_3$ thin films for the grain growth study are prepared on Si substrates. For material characterizations such as AFM, SEM, XRD, and STEM, an unstructured Si stamp (i.e., flat-stamp) is used in NIL.

To prepare the unstructured NIL stamp, an immaculate Si substrate is used, and the Si substrate is coated with an anti-adhesion monolayer of perfluorodecyltrichlorosilane (FDTS) (from Alfa Aesar). After confirming the hydrophobicity of the stamp (e.g., the contact angle between the water droplet and the stamp is higher than 100°) using a Rame-Hart goniometer, NIL is performed with an Obducat nanoimprinter. We place one Al foil with an O-ring to hold the stamp in place on top of the film by turning on vacuum. After ensuring that the vacuum is holding the stamp in place, we remove the O-ring and place one poly foil on top of the stack (Al foil/stamp/film). The time in maintaining the set temperature (e.g., 60, 100, or 120 °C) is defined as the imprint time (e.g., 10, 20, or 40 min) in our study. In the case of the low-pressure NIL test, 10 bar pressure is maintained during the heat-up time to the set temperature. For the high-pressure NIL test, pressure is gradually increased from 10 to 70 bar pressure during the heat-up time. The NIL process is finished with demolding of the stamp from the film after the nanoimprinter system cools down and pressure is released to the atmosphere. Figure S1 illustrates the NIL process and the deformation of the perovskite film by NIL at different temperatures and pressures.

In order to prepare three different PeLECs (without NIL, flat-NIL, and nanohole-NIL), $MAPbBr_3$ thin films with a thickness of 190 nm are spin coated on immaculate ITO/glass substrates [Liasion Quartz (Lianyungang Jiangsu China), sheet resistance ~15 Ω sq^{-1}]. For PeLECs with flat-NIL and nanohole-NIL, the 100 °C, 70 bar, and 20 min NIL process is employed with FDTS-coated flat stamp and commercially available 2D nanopillar stamp (Lightsmyth).

SEM, AFM, STEM, and TEM–EDX. Morphology examination is first carried out by taking SEM images since SEM is a better sampling imaging method than AFM and STEM. SEM images are taken using 30 μm aperture size and an in-lens detector at a working distance of 3–4 mm and an accelerating voltage of 6–10 kV using a Zeiss Supra-40 scanning electron microscope. Due to the ultra-smooth surface of our $MAPbBr_3$ films, SEM cannot resolve the subtle variation in height (e.g., roughness) among the films that underwent different NIL processes. Since AFM has a much better vertical resolution (<0.5 Å) and measures both vertical and lateral dimensions of the film with a single scan,[56] AFM images are taken for a 2 μm × 2 μm area using the tapping mode using a Veeco Dimension 5000 SPM. To observe defects within and on the surface of grains using STEM, free-standing $MAPbBr_3$ films are prepared by scrapping with a razor blade, and the scrapped films are dispersed in toluene by ultrasonication. A holey and thin carbon film (double layers)-coated copper 200 mesh grid (Cu-200 HD) is employed for the droplet of dispersed $MAPbBr_3$ films. After drying off the toluene, STEM and TEM–EDX measurements are carried out using an aberration-corrected JEM-ARM200F (from JEOL USA Inc.) at an accelerating voltage of 200 kV.

X-ray Diffraction. To examine the crystal structure, crystallinity, and texture development of $MAPbBr_3$ thin films, four different XRD measurement techniques, including out-of-plane, in-plane, omega rocking curve, and pole figure, are carried out using a Rigaku SmartLab X-ray diffractometer with a Cu target (Ka1 = 1.54059 Å) and a HyPix 3000 detector.

X-ray Photoelectron Spectroscopy. XPS was used for the elemental compositional analysis of the sample surface. XPS measurements were performed on perovskite thin films using a Versa Probe II at an ultrahigh vacuum of 10^{-8} Pa. The X-ray source used is Al Kα, which has 1486.6 eV photon energy, 50 W gun power, 15 kV operating voltage, 200 μm X-ray spot size, and 59° angle between the X-ray source and detector. Before obtaining the XPS data, calibration using internal standard Au, Cu, and Ag samples was performed. XPS data were obtained with six sweeps at a pass energy of 187.85 eV, and high-resolution XPS data for each element were obtained with six sweeps at a pass energy of 23.5 eV.

Steady-State Photoluminescence Spectroscopy. Photoluminescence (PL) spectra are measured with a spectrograph (Princeton Instruments, IsoPlane SCT-320) coupled to a cooled Si detector (Princeton Instruments, PIXIS:400BRX), with each $MAPbBr_3$ film optically pumped using a nanosecond pulsed 355 nm laser (TALON-355-20, Spectra-Physics).

LEC Measurement. All measurements are conducted using a mechanical probe station under high vacuum <20 mTorr. Current density–voltage (J–V) and luminance–voltage (L–V) characteristics

https://dx.doi.org/10.1021/acsami.0c17655
ACS Appl. Mater. Interfaces 2021, 13, 5368–5378

are measured using a Keithley 2400 source meter and a Photo Research PR-650 spectroradiometer in the range of 0−5 V with 0.5 V increment.

Surface Energy Calculation. To estimate surface energies with different surface orientations, we carry out the first-principles calculations based on DFT[57,58] using Vienna Ab initio Simulation Package (VASP).[59,60] For the exchange−correlation energy, we adopt the Perdew−Burke−Ernzerhof functional[61] in the generalized gradient approximation. Pseudopotentials are given by the projector-augmented wave method.[62,63] Also, the 5*d* orbital is included in Pb valence. The energy cutoff for the plane-wave basis set is set to 400 eV, and spin-polarized calculations are performed. A Monkhorst−Pack *k*-point grid of 4 × 4 × 1 is adopted for the Brillouin zone sampling. The simulation domain includes a 15 Å-thick vacuum region, and geometry is relaxed with a fixed cell shape and volume.

The surface energy γ is calculated using

$$\gamma = \left(E_{\text{slab}} - \sum_i n_i \mu_i\right)/2A \tag{1}$$

where E_{slab} is the total energy of a slab system, n_i is the number of atoms of a species i, μ_i is the chemical potential of a species i in the bulk phase, and A is the surface area.

Given competing phases—MABr and $PbBr_2$—chemical potentials of each species in $MAPbBr_3$ are determined in the following relationships[64]

$$\mu_{\text{MA}} + \mu_{\text{Pb}} + 3\mu_{\text{Br}} = \mu_{\text{MAPbBr}_3} \tag{2}$$

$$\mu_{\text{MA}} + \mu_{\text{Br}} < \mu_{\text{MABr}} \tag{3}$$

$$\mu_{\text{Pb}} + 2\mu_{\text{Br}} < \mu_{\text{PbBr}_2} \tag{4}$$

Note that the chemical potentials have a range rather than a single quantity.

To determine the chemical potentials for each element, we specify Pb-rich conditions that have been observed in the TEM−EDX and XPS experiment. After some algebra, in the Pb-rich conditions, the chemical potentials are derived as in

$$\mu_{\text{Pb}} = \mu_{\text{Pb,bulk}} \tag{5}$$

$$\frac{\mu_{\text{MAPbBr}_3} - \mu_{\text{MABr}} - \mu_{\text{Pb}}}{2} < \mu_{\text{Br}} < \frac{\mu_{\text{PbBr}_2} - \mu_{\text{Pb}}}{2} \tag{6}$$

$$\frac{2\mu_{\text{MAPbBr}_3} - 3\mu_{\text{PbBr}_2} + \mu_{\text{Pb}}}{2} < \mu_{\text{MA}} < \frac{3\mu_{\text{MABr}} - \mu_{\text{MAPbBr}_3} + \mu_{\text{Pb}}}{2} \tag{7}$$

The chemical potentials of the compounds are extracted from solid phases at 0 K except for μ_{MABr}, which is obtained from an isolated MA−Br.

■ ASSOCIATED CONTENT

Supporting Information

The Supporting Information is available free of charge at https://pubs.acs.org/doi/10.1021/acsami.0c17655.

Schematic of the NIL process and the effect of pressure and temperature, AFM images of $MAPbBr_3$ thin films that underwent different processing conditions, SEM images of 120 °C and 70 bar processed, 100 °C and 70 bar processed, and two month-old $MAPbBr_3$ thin films, analysis of XRD peak locations from $MAPbBr_3$ thin films with and without NIL using out-of-plane and in-plane XRD techniques, PL spectra of $MAPbBr_3$ thin films that underwent different processing conditions, out-of-plane XRD scanned from 5 to 60° and high-angle annular dark-field (HAADF) STEM images of $MAPbBr_3$ thin films with and without NIL, histograms of grain size distribution without and with NIL, SEM images of near-zero residual NIL nanohole patterns, high-angle annular bright-field (HAABF) STEM images and TEM−EDX measurements on $MAPbBr_3$ thin films with and without NIL, and XPS measurements on $MAPbBr_3$ thin films with and without NIL (PDF)

■ AUTHOR INFORMATION

Corresponding Author

Qing Gu − *Department of Electrical and Computer Engineering, The University of Texas at Dallas, Richardson, Texas 75080, United States;* orcid.org/0000-0003-3855-3690; Email: qing.gu@utdallas.edu

Authors

Jiyoung Moon − *Department of Materials Science and Engineering, The University of Texas at Dallas, Richardson, Texas 75080, United States*

Sunah Kwon − *Department of Materials Science and Engineering, The University of Texas at Dallas, Richardson, Texas 75080, United States*

Masoud Alahbakhshi − *Department of Electrical and Computer Engineering, The University of Texas at Dallas, Richardson, Texas 75080, United States*

Yeonghun Lee − *Department of Materials Science and Engineering, The University of Texas at Dallas, Richardson, Texas 75080, United States*

Kyeongjae Cho − *Department of Materials Science and Engineering, The University of Texas at Dallas, Richardson, Texas 75080, United States;* orcid.org/0000-0003-2698-7774

Anvar Zakhidov − *Department of Physics, The University of Texas at Dallas, Richardson, Texas 75080, United States; Department of Nanophotonics and Metamaterials, ITMO University, St. Petersburg 197101, Russia;* orcid.org/0000-0003-3983-2229

Moon J. Kim − *Department of Materials Science and Engineering, The University of Texas at Dallas, Richardson, Texas 75080, United States*

Complete contact information is available at: https://pubs.acs.org/10.1021/acsami.0c17655

Author Contributions

Q.G. and J.M. conceived the project idea; J.M. designed the experiments under the guidance of Q.G.; M.A. prepared the thin films; J.M. conducted the NIL, AFM, SEM, XPS, and PL measurements; M.A. fabricated PeLECs and performed the EL measurements; J.M. conducted the XRD measurements with the help of S.K.; S.K. conducted the STEM and TEM measurements; J.M. carried out the post-processing of optical and material characterization results; Y.L. and K.C. performed DFT calculations; J.M. and Q.G. wrote the manuscript. All authors participated in the data analysis and the improvement of the manuscript.

Notes

The authors declare no competing financial interest.

■ ACKNOWLEDGMENTS

This work is supported by the Welch Foundation (grants AT-1992-20190330 and AT-1617), National Science Foundation (NSF) CAREER Award (ECCS-1941629), The University of Texas at Dallas Office of Research through the SPIRe Grant

Program, National Research Foundation (NRF) of Korea by Creative Materials Discovery Program (2015M3D1A1068062), Nano Materials Technology Development Program (2016M3A7B4909942), and the Louis Beecherl, Jr. endowment fund. Y.L. and K.C. acknowledge the Texas Advanced Computing Center (TACC) for providing supercomputing resources.

REFERENCES

(1) Sutherland, B. R.; Sargent, E. H. Perovskite Photonic Sources. *Nat. Photonics* **2016**, *10*, 295−302.
(2) Liao, Q.; Jin, X.; Fu, H. Tunable Halide Perovskites for Miniaturized Solid-State Laser Applications. *Adv. Opt. Mater.* **2019**, *7*, 1900099.
(3) Kumawat, N. K.; Liu, X.-K.; Kabra, D.; Gao, F. Blue Perovskite Light-Emitting Diodes: Progress, Challenges and Future Directions. *Nanoscale* **2019**, *11*, 2109−2120.
(4) Jung, M.; Ji, S.-G.; Kim, G.; Seok, S. I. Perovskite Precursor Solution Chemistry: From Fundamentals to Photovoltaic Applications. *Chem. Soc. Rev.* **2019**, *48*, 2011−2038.
(5) Li, Z.; Moon, J.; Gharajeh, A.; Haroldson, R.; Hawkins, R.; Hu, W.; Zakhidov, A.; Gu, Q. Roomerature Continuous-Wave Operation of Organometal Halide Perovskite Lasers. *ACS Nano* **2018**, *12*, 10968−10976.
(6) Chen, S.; Roh, K.; Lee, J.; Chong, W. K.; Lu, Y.; Mathews, N.; Sum, T. C.; Nurmikko, A. A Photonic Crystal Laser from Solution Based Organo-Lead Iodide Perovskite Thin Films. *ACS Nano* **2016**, *10*, 3959−3967.
(7) Jia, Y.; Kerner, R. A.; Grede, A. J.; Brigeman, A. N.; Rand, B. P.; Giebink, N. C. Diode-Pumped Organo-Lead Halide Perovskite Lasing in a Metal-Clad Distributed Feedback Resonator. *Nano Lett.* **2016**, *16*, 4624−4629.
(8) Cha, H.; Bae, S.; Lee, M.; Jeon, H. Two-Dimensional Photonic Crystal Bandedge Laser with Hybrid Perovskite Thin Film for Optical Gain. *Appl. Phys. Lett.* **2016**, *108*, 181104.
(9) Pourdavoud, N.; Haeger, T.; Mayer, A.; Cegielski, P. J.; Giesecke, A. L.; Heiderhoff, R.; Olthof, S.; Zaefferer, S.; Shutsko, I.; Henkel, A.; Becker-Koch, D.; Stein, M.; Cehovski, M.; Charfi, O.; Johannes, H. H.; Rogalla, D.; Lemme, M. C.; Koch, M.; Vaynzof, Y.; Meerholz, K.; Kowalsky, W.; Scheer, H. C.; Görrn, P.; Riedl, T. Room-Temperature Stimulated Emission and Lasing in Recrystallized Cesium Lead Bromide Perovskite Thin Films. *Adv. Mater.* **2019**, *31*, No. e1903717.
(10) Bar-On, O.; Brenner, P.; Lemmer, U.; Scheuer, J. Micro Lasers by Scalable Lithography of Metal-Halide Perovskites. *Adv. Mater. Technol.* **2018**, *3*, 1800212.
(11) Huang, C.; Zhang, C.; Xiao, S.; Wang, Y.; Fan, Y.; Liu, Y.; Zhang, N.; Qu, G.; Ji, H.; Han, J.; Ge, L.; Kivshar, Y.; Song, Q. Ultrafast Control of Vortex Microlasers. *Science* **2020**, *367*, 1018−1021.
(12) Wang, S.; Liu, Y.; Li, G.; Zhang, J.; Zhang, N.; Xiao, S.; Song, Q. Lead Halide Perovskite Based Microdisk Lasers for On-Chip Integrated Photonic Circuits. *Adv. Opt. Mater.* **2018**, *6*, 1701266.
(13) Pourdavoud, N.; Mayer, A.; Buchmüller, M.; Brinkmann, K.; Häger, T.; Hu, T.; Heiderhoff, R.; Shutsko, I.; Görrn, P.; Chen, Y.; Scheer, H.-C.; Riedl, T. Distributed Feedback Lasers Based on MAPbBr3. *Adv. Mater. Technol.* **2018**, *3*, 1700253.
(14) Pourdavoud, N.; Wang, S.; Mayer, A.; Hu, T.; Chen, Y.; Marianovich, A.; Kowalsky, W.; Heiderhoff, R.; Scheer, H.-C.; Riedl, T. Photonic Nanostructures Patterned by Thermal Nanoimprint Directly into Organo-Metal Halide Perovskites. *Adv. Mater.* **2017**, *29*, 1605003.
(15) Zhao, T.; Liu, H.; Ziffer, M. E.; Rajagopal, A.; Zuo, L.; Ginger, D. S.; Li, X.; Jen, A. K. Y. Realization of a Highly Oriented MAPbBr3 Perovskite Thin Film via Ion Exchange for Ultrahigh Color Purity Green Light Emission. *ACS Energy Lett.* **2018**, *3*, 1662−1669.
(16) Lin, K.; Xing, J.; Quan, L. N.; de Arquer, F. P. G.; Gong, X.; Lu, J.; Xie, L.; Zhao, W.; Zhang, D.; Yan, C.; Li, W.; Liu, X.; Lu, Y.; Kirman, J.; Sargent, E. H.; Xiong, Q.; Wei, Z. Perovskite Light-Emitting Diodes with External Quantum Efficiency Exceeding 20 per Cent. *Nature* **2018**, *562*, 245−248.
(17) Mao, J.; Sha, W. E. I.; Zhang, H.; Ren, X.; Zhuang, J.; Roy, V. A. L.; Wong, K. S.; Choy, W. C. H. Novel Direct Nanopatterning Approach to Fabricate Periodically Nanostructured Perovskite for Optoelectronic Applications. *Adv. Funct. Mater.* **2017**, *27*, 1606525.
(18) Alahbakhshi, M.; Mishra, A.; Haroldson, R.; Ishteev, A.; Moon, J.; Gu, Q.; Slinker, J. D.; Zakhidov, A. A. Bright and Effectual Perovskite Light-Emitting Electrochemical Cells Leveraging Ionic Additives. *ACS Energy Lett.* **2019**, *4*, 2922−2928.
(19) Aygüler, M. F.; Weber, M. D.; Puscher, B. M. D.; Medina, D. D.; Docampo, P.; Costa, R. D. Light-Emitting Electrochemical Cells Based on Hybrid Lead Halide Perovskite Nanoparticles. *J. Phys. Chem. C* **2015**, *119*, 12047−12054.
(20) Mishra, A.; Alahbakhshi, M.; Haroldson, R.; Bastatas, L. D.; Gu, Q.; Zakhidov, A. A.; Slinker, J. D. Enhanced Operational Stability of Perovskite Light-Emitting Electrochemical Cells Leveraging Ionic Additives. *Adv. Opt. Mater.* **2020**, *8*, 2000226.
(21) Chen, A. Z.; Foley, B. J.; Ma, J. H.; Alpert, M. R.; Niezgoda, J. S.; Choi, J. J. Crystallographic Orientation Propagation in Metal Halide Perovskite Thin Films. *J. Mater. Chem. A* **2017**, *5*, 7796−7800.
(22) Fu, X.; Dong, N.; Lian, G.; Lv, S.; Zhao, T.; Wang, Q.; Cui, D.; Wong, C.-P. High-Quality CH3NH3PbI3 Films Obtained via a Pressure-Assisted Space-Confined Solvent-Engineering Strategy for Ultrasensitive Photodetectors. *Nano Lett.* **2018**, *18*, 1213−1220.
(23) Zhang, W.; Saliba, M.; Moore, D. T.; Pathak, S. K.; Hörantner, M. T.; Stergiopoulos, T.; Stranks, S. D.; Eperon, G. E.; Alexander-Webber, J. A.; Abate, A.; Sadhanala, A.; Yao, S.; Chen, Y.; Friend, R. H.; Estroff, L. A.; Wiesner, U.; Snaith, H. J. Ultrasmooth Organic-Inorganic Perovskite Thin-Film Formation and Crystallization for Efficient Planar Heterojunction Solar Cells. *Nat. Commun.* **2015**, *6*, 6142.
(24) Ji, C.; Liang, C.; Zhang, H.; Sun, M.; Song, Q.; Sun, F.; Feng, X.; Liu, N.; Gong, H.; Li, D.; You, F.; He, Z.; Sharenko, A.; Toney, M. F.; Dong, Q.; Yuan, Y.; Shao, Y.; Fang, Y.; Wang, Q.; Huang, J.; Yao, Z.; Wang, W.; Shen, H.; Zhang, Y.; Luo, Q.; Yin, X.; Dai, X.; Li, J.; Lin, H.; Wei, D.; Ji, J.; Song, D.; Li, M.; Cui, P.; Li, Y.; Mbengue, J. M.; Zhou, W.; Ning, Z.; Park, N. Secondary Grain Growth in Organic−Inorganic Perovskite Films with Ethylamine Hydrochloride Additives for Highly Efficient Solar Cells. *ACS Appl. Mater. Interfaces* **2020**, *12*, 20026−20034.
(25) Noel, N. K.; Abate, A.; Stranks, S. D.; Parrott, E. S.; Burlakov, V. M.; Goriely, A.; Snaith, H. J. Enhanced Photoluminescence and Solar Cell Performance via Lewis Base Passivation of Organic-Inorganic Lead Halide Perovskites. *ACS Nano* **2014**, *8*, 9815−9821.
(26) Sahli, F.; Werner, J.; Kamino, B. A.; Bräuninger, M.; Monnard, R.; Paviet-Salomon, B.; Barraud, L.; Ding, L.; Diaz Leon, J. J.; Sacchetto, D.; Cattaneo, G.; Despeisse, M.; Boccard, M.; Nicolay, S.; Jeangros, Q.; Niesen, B.; Ballif, C. Fully Textured Monolithic Perovskite/Silicon Tandem Solar Cells with 25.2% Power Conversion Efficiency. *Nat. Mater.* **2018**, *17*, 820−826.
(27) Wang, H.; Haroldson, R.; Balachandran, B.; Zakhidov, A.; Sohal, S.; Chan, J. Y.; Zakhidov, A.; Hu, W. Nanoimprinted Perovskite Nanograting Photodetector with Improved Efficiency. *ACS Nano* **2016**, *10*, 10921−10928.
(28) Kim, W.; Jung, M. S.; Lee, S.; Choi, Y. J.; Kim, J. K.; Chai, S. U.; Kim, W.; Choi, D.-G.; Ahn, H.; Cho, J. H.; Choi, D.; Shin, H.; Kim, D.; Park, J. H. Oriented Grains with Preferred Low-Angle Grain Boundaries in Halide Perovskite Films by Pressure-Induced Crystallization. *Adv. Energy Mater.* **2018**, *8*, 1702369.
(29) Chou, S. S.; Swartzentruber, B. S.; Janish, M. T.; Meyer, K. C.; Biedermann, L. B.; Okur, S.; Burckel, D. B.; Carter, C. B.; Kaehr, B. Laser Direct Write Synthesis of Lead Halide Perovskites. *J. Phys. Chem. Lett.* **2016**, *7*, 3736−3741.
(30) Wei, D.; Ji, J.; Song, D.; Li, M.; Cui, P.; Li, Y.; Mbengue, J. M.; Zhou, W.; Ning, Z.; Park, N.-G. A TiO2 Embedded Structure for Perovskite Solar Cells with Anomalous Grain Growth and Effective Electron Extraction. *J. Mater. Chem. A* **2017**, *5*, 1406−1414.

https://dx.doi.org/10.1021/acsami.0c17655
ACS Appl. Mater. Interfaces 2021, 13, 5368−5378

(31) Sharenko, A.; Toney, M. F. Relationships between Lead Halide Perovskite Thin-Film Fabrication, Morphology, and Performance in Solar Cells. *J. Am. Chem. Soc.* **2016**, *138*, 463−470.
(32) Dong, Q.; Yuan, Y.; Shao, Y.; Fang, Y.; Wang, Q.; Huang, J. Abnormal Crystal Growth in CH3NH3PbI3-XClx Using a Multi-Cycle Solution Coating Process. *Energy Environ. Sci.* **2015**, *8*, 2464−2470.
(33) Yao, Z.; Wang, W.; Shen, H.; Zhang, Y.; Luo, Q.; Yin, X.; Dai, X.; Li, J.; Lin, H. CH 3 NH 3 PbI 3 Grain Growth and Interfacial Properties in Meso-Structured Perovskite Solar Cells Fabricated by Two-Step Deposition. *Sci. Technol. Adv. Mater.* **2017**, *18*, 253−262.
(34) Huang, X.; Bi, W.; Jia, P.; Cui, Q.; Hu, Y.; Lou, Z.; Hou, Y.; Teng, F. Grain Growth of MAPbI3 via Diethylammonium Bromide Induced Grain Mergence. *ACS Appl. Mater. Interfaces* **2020**, *12*, 16707−16714.
(35) Brittman, S.; Oener, S. Z.; Guo, K.; Āboliņš, H.; Koenderink, A. F.; Garnett, E. C. Controlling Crystallization to Imprint Nanophotonic Structures into Halide Perovskites Using Soft Lithography. *J. Mater. Chem. C* **2017**, *5*, 8301−8307.
(36) Lyashenko, D.; Perez, A.; Zakhidov, A. High-Resolution Patterning of Organohalide Lead Perovskite Pixels for Photodetectors Using Orthogonal Photolithography. *Phys. Status Solidi A* **2017**, *214*, 1600302.
(37) Gao, Y.; Huang, C.; Hao, C.; Sun, S.; Zhang, L.; Zhang, C.; Duan, Z.; Wang, K.; Jin, Z.; Zhang, N.; Kildishev, A. V.; Qiu, C.-W.; Song, Q.; Xiao, S. Lead Halide Perovskite Nanostructures for Dynamic Color Display. *ACS Nano* **2018**, *12*, 8847−8854.
(38) Wang, T.; Lian, G.; Huang, L.; Zhu, F.; Cui, D.; Wang, Q.; Meng, Q.; Wong, C.-P. MAPbI3Quasi-Single-Crystal Films Composed of Large-Sized Grains with Deep Boundary Fusion for Sensitive Vis-NIR Photodetectors. *ACS Appl. Mater. Interfaces* **2020**, *12*, 38314−38324.
(39) Yang, J.; Siempelkamp, B. D.; Liu, D.; Kelly, T. L. Investigation of CH3NH3PbI3degradation Rates and Mechanisms in Controlled Humidity Environments Using in Situ Techniques. *ACS Nano* **2015**, *9*, 1955−1963.
(40) Yi, N.; Wang, S.; Duan, Z.; Wang, K.; Song, Q.; Xiao, S. Tailoring the Performances of Lead Halide Perovskite Devices with Electron-Beam Irradiation. *Adv. Mater.* **2017**, *29*, 1701636.
(41) Melvin, A. A.; Stoichkov, V. D.; Kettle, J.; Mogilyansky, D.; Katz, E. A.; Visoly-Fisher, I. Lead Iodide as a Buffer Layer in UV-Induced Degradation of CH3NH3PbI3films. *Sol. Energy* **2018**, *159*, 794−799.
(42) Alias, M. S.; Yang, Y.; Ng, T. K.; Dursun, I.; Shi, D.; Saidaminov, M. I.; Priante, D.; Bakr, O. M.; Ooi, B. S. Enhanced Etching, Surface Damage Recovery, and Submicron Patterning of Hybrid Perovskites Using a Chemically Gas-Assisted Focused-Ion Beam for Subwavelength Grating Photonic Applications. *J. Phys. Chem. Lett.* **2016**, *7*, 137−142.
(43) Kanaujia, P. K.; Vijaya Prakash, G. Laser-Induced Microstructuring of Two-Dimensional Layered Inorganic-Organic Perovskites. *Phys. Chem. Chem. Phys.* **2016**, *18*, 9666−9672.
(44) Jeong, B.; Hwang, I.; Cho, S. H.; Kim, E. H.; Cha, S.; Lee, J.; Kang, H. S.; Cho, S. M.; Choi, H.; Park, C. Solvent-Assisted Gel Printing for Micropatterning Thin Organic-Inorganic Hybrid Perovskite Films. *ACS Nano* **2016**, *10*, 9026−9035.
(45) Mayer, A.; Buchmüller, M.; Wang, S.; Steinberg, C.; Papenheim, M.; Scheer, H.-C.; Pourdavoud, N.; Haeger, T.; Riedl, T. Thermal Nanoimprint to Improve the Morphology of $MAPbX_3$ (MA = Methylammonium, X = I or Br). *J. Vac. Sci. Technol., B: Microelectron. Nanometer Struct.–Process., Meas., Phenom.* **2017**, *35*, 06G803.
(46) Heiderhoff, R.; Haeger, T.; Pourdavoud, N.; Hu, T.; Al-Khafaji, M.; Mayer, A.; Chen, Y.; Scheer, H.-C.; Riedl, T. Thermal Conductivity of Methylammonium Lead Halide Perovskite Single Crystals and Thin Films—A Comparative Study. *J. Phys. Chem. C* **2017**, *121*, 28306−28311.
(47) Wang, Y.; He, J.; Chen, H.; Chen, J.; Zhu, R.; Ma, P.; Towers, A.; Lin, Y.; Gesquiere, A. J.; Wu, S.-T.; Dong, Y. Ultrastable, Highly Luminescent Organic-Inorganic Perovskite-Polymer Composite Films. *Adv. Mater.* **2016**, *28*, 10710−10717.
(48) Chou, S. Y.; Krauss, P. R.; Renstrom, P. J. Imprint of Sub-25 Nm Vias and Trenches in Polymers. *Appl. Phys. Lett.* **1995**, *67*, 3114.
(49) Stoumpos, C. C.; Malliakas, C. D.; Kanatzidis, M. G. Semiconducting Tin and Lead Iodide Perovskites with Organic Cations: Phase Transitions, High Mobilities, and near-Infrared Photoluminescent Properties. *Inorg. Chem.* **2013**, *52*, 9019−9038.
(50) Dimesso, L.; Dimamay, M.; Hamburger, M.; Jaegermann, W. Properties of CH3NH3PbX3 (X = I, Br, Cl) Powders as Precursors for Organic/Inorganic Solar Cells. *Chem. Mater.* **2014**, *26*, 6762−6770.
(51) Weale, F. E. On the Growth of Language. *Broadway* **1947**, *11*, 114−116.
(52) Thompson, C. V. Grain Growth in Thin Films. *Annu. Rev. Mater. Sci.* **1990**, *20*, 245−268.
(53) Thompson, C. V.; Carel, R. Texture Development in Polycrystalline Thin Films. *Mater. Sci. Eng., B* **1995**, *32*, 211−219.
(54) Widjonarko, N. Introduction to Advanced X-Ray Diffraction Techniques for Polymeric Thin Films. *Coatings* **2016**, *6*, 54.
(55) Nagao, K.; Kagami, E. X-Ray Thin Film Measurement Techniques: VII. Pole Figure Measurement. *Rigaku J.* **2011**, *27*, 6−14.
(56) Russell, P.; Batchelor, D.; Thornton, J. SEM and AFM : Complementary Techniques for Surface Investigations. *Microsc. Anal.* **2001**, 9−12.
(57) Hohenberg, P.; Kohn, W. Inhomogeneous Electron Gas. *Phys. Rev.* **1964**, *136*, B864.
(58) Kohn, W.; Sham, L. J. Self-Consistent Equations Including Exchange and Correlation Effects. *Phys. Rev.* **1965**, *140*, A1133.
(59) Kresse, G.; Furthmüller, J. Efficiency of Ab-Initio Total Energy Calculations for Metals and Semiconductors Using a Plane-Wave Basis Set. *Comput. Mater. Sci.* **1996**, *6*, 15−50.
(60) Kresse, G.; Furthmüller, J. Efficient Iterative Schemes for Ab Initio Total-Energy Calculations Using a Plane-Wave Basis Set. *Phys. Rev. B: Condens. Matter Mater. Phys.* **1996**, *54*, 11169−11186.
(61) Perdew, J. P.; Burke, K.; Ernzerhof, M. Generalized Gradient Approximation Made Simple [Phys. Rev. Lett. 77, 3865 (1996)]. *Phys. Rev. Lett.* **1997**, *78*, 1396.
(62) Blöchl, P. E. Projector Augmented-Wave Method. *Phys. Rev. B: Condens. Matter Mater. Phys.* **1994**, *50*, 17953.
(63) Kresse, G.; Joubert, D. From Ultrasoft Pseudopotentials to the Projector Augmented-Wave Method. *Phys. Rev. B: Condens. Matter Mater. Phys.* **1999**, *59*, 1758.
(64) Huang, X.; Paudel, T. R.; Dowben, P. A.; Dong, S.; Tsymbal, E. Y. Electronic structure and stability of the CH3NH3PbBr3 (001) surface. *Phys. Rev. B* **2016**, *94*, 195309.

https://dx.doi.org/10.1021/acsami.0c17655
ACS Appl. Mater. Interfaces 2021, 13, 5368−5378